Source Localization of Microseismic Emissions during Pneumatic Fracturing

Antoine L. Turquet[1]*, Renaud Toussaint[1,2,3], Fredrik Kvalheim Eriksen[1,2], Guillaume Daniel[4], Olivier Lengliné[1,3], Eirik G. Flekkøy[2,3],Knut Jørgen Måløy[2,3]

[1]University of Strasbourg, Institut de Physique du Globe de Strasbourg, CNRS UMR7516, 5 Rue Descartes, F-67000 Strasbourg, France

[2]SFF PoreLab, The Njord Centre, Department of Physics, University of Oslo, PO Box 1048, Blindern, N-0316, Oslo, Norway

[3]International Associate Laboratory LIA D-FFRACT, Deformation, Flow and Fracture of Disordered Materials, France-Norway

[4]EDF - Direction Industrielle, Aix-en-Provence, France

Key Points:

- The pneumatic fracturing experiments in a Hele-Shaw cell are monitored using accelerometers and a high speed camera.
- The acoustic emissions are localized using an energy based signal location method and displacement maps are obtained from image correlation.
- By comparing the acoustic and the optical results we observe the motion starts in porous medium and propagates towards the channel tips.

*Currently working at ENS Lyon, France

Abstract

Localization of signals is a widely applied technique used in different areas of science telecommunication, medicine or seismology. In this work, we study microseismic emissions due to stick-slip events during pneumatic fracture in a transparent setup at laboratory scale and apply a localization method "Estimated Source Energy Homogeneity". The seismic location results are compared with the image correlation results for displacement maps corresponding to the event times. We have observed (using optics and acoustics) that the movement starts inside the porous medium and progresses towards the channel tips, eventually causing channels to grow further. This finding could be of interest in understanding fluid-induced earthquake nucleation processes. Similar to in-site applications of pneumatic or fluid-related fracturing, it shows that the area influenced extends beyond the fracture tips. This also shows why even after the end of pumping, we may get earthquakes, such as in the Basel case [Haring et al. 2008].

1 Introduction

Acoustic signal localization is applied in many different areas of science [*Gershman et al.*, 1995; *Valin et al.*, 2003; *Elnahrawy et al.*, 2004; *Malioutov et al.*, 2005; *Zhu et al.*, 2007; *Fink*, 2015; *Garnier and Fink*, 2015]. In robotics, speech-source tracking is done to automate cameras to follow the speaker [*Brandstein et al.*, 1997]. In electronics, touchscreens are a very popular example of a signal localization. It is necessary for the system to locate the touch of a user to transmit information to process a simple message [*Terlizzi and Minoo*, 2009].

Similarly, in earth sciences, finding the epicenter of an earthquake is necessary to understand how it was generated, where exactly the movement occurred, which region is more risky for the aftershocks [*Aki and Richards*, 2002], [*Turquet et al.*, 2018a]. For a better quality risk assessment, it is important to know the origin of the seismicity along with its location. In nature, seismic events based on gas-solid interactions are very common. For example, there are many existing studies about a volcano-heated fluid becomes gas causing phreatic eruptions or geysers [*Tazieff*, 1989; *Oppenheimer*, 1986; *Manga and Brodsky*, 2006; *Christenson et al.*, 2010; *Jolly et al.*, 2014; *Sudo et al.*, 1998]. Moreover, fast air or fluid injection deforming porous medium is used in the industrial applications of pneumatic fracturing [*Schuring et al.*, 1996; *Accutech*, 1994; *Gao et al.*, 2014] or hydraulic fracturing [*Charléty et al.*, 2007; *Cuenot et al.*, 2008; *Dorbath et al.*, 2009; *Aochi*

et al., 2011]. At very large scales (tens or hundreds of meters) and high-pressure injection, compressibility plays role in the interactions between the pressurized fluid and deformable solid medium similar to the gas-solid interactions mentioned earlier. This physical phenomenon can be observed in magma fracturing, eruptions [*Rivalta and Segall*, 2007; *Poland et al.*, 2012], fluid injecting into rocks, or reservoir stimulations in geothermal fields [*Candela et al.*, 2018]. *Stanchits et al.* [2011] have studied the acoustic emissions on rock samples during thermo-hydro-chemo-mechanical coupled deformations. Water injection into porous sandstone under applied stress induced acoustic emission events. These events are generated close to the migrating waterfront. *Kobchenko et al.* [2013] studied the transport of CO_2 by diffusion and fracturing the gel layer in a Hele-Shaw cell. They studied the length scales of diffusion and flow in fracture networks which are eventually linked to statistical properties of river networks and hierarchical-fracture networks. In the very recent research of *Jamtveit et al.* [2018], they have found that the strike-slip lower crust earthquakes are causing fluid pressure pulses towards the lower crust and fluid-driven associated metamorphic and structural transformations of the lower crust follow these earthquakes. More importantly, at large scales, a common way to understand and control the fluid induced fracturing is to monitor the microseismicity [*Holland*, 2013; *Valkó and Economides*, 1995; *Cornet et al.*, 1998; *Cornet*, 2015; *Fehler et al.*]. The source locations of seismic events are mainly focusing on the fluid-solid coupled events.

Even though the localization of the microseismicity due to volcanoes, and industrial applications such as hydraulic fracturing has a very rich scientific literature, the locations of acoustic emissions based on interactions between the injected gas and deformable the solid (or gas-metal in pressure tanks [*Peacock*, 1996]) remains challenging. To the best of our knowledge, acoustic emissions have not been studied during pneumatic fractures in the scientific literature prior to this article. In this article, we are investigating the source mechanics and locations of pneumatic fractures in a porous medium in a transparent Hele-Shaw cell. The main focus of this work is to first locate the stick-slip events using acoustic emissions and then to compare them with the displacement field obtained from digital image correlation. The main reason behind using a Hele-Shaw cell is to optically record the deformations associated with the microseismic event while recording the vibrations on the glass plate with accelerometers. This work is based on the similar experiments as in the previous works done by *Turkaya et al.* [2015], *Eriksen et al.* [2017a], *Eriksen et al.* [2018], and *Turquet et al.* [2018b].

Recently, some of the signal localization types are reviewed in the work *Turkaya et al.* [2016]. Here in this article, we show the application of Estimation of Source Energy Homogeneity (ESEH) to locate the source of the acoustic emissions during aerofracturing experiments [*Turkaya et al.*, 2015]. These localization results are compared with the Digital Image Correlation (details can be found in *Eriksen et al.* [2017a] results), as obtained from the optical recordings via a high-speed camera during the experiment.

2 Experimental setup

The aerofracturing experiments analyzed here are conducted in a Hele-Shaw cell made of two glass plates 80 cm $\times$ 40 cm $\times$ 1 cm with an aperture of 1 mm between them - see details in *Turkaya et al.* [2015], *Eriksen et al.* [2017b], *Eriksen et al.* [2018], and *Turquet et al.* [2018b]. The experimental setup is shown in Figure 1(a). The acquisition chains of optical and acoustic data are presented. The system is triggered via a signal generator to have synchronization between optical and acoustic data. The optical data were recorded at 125 or 1000 images per second using a Photron SA5 and a flicker-free Dedolight 400W projector, and for acoustic data, we use 1 MHz sampling rate. Three boundaries of this cell are sealed with a double-sided tape while the fourth side is covered with a 40 μm mesh filter. This filter lets the air pass to the surrounding atmosphere while keeping the grains inside of the cell. In this particular experiment, we used 1 bar overpressure from the inlet and we used 80 μm grains having material density 1.05 g/cm^3 in loose state inside the cell. Prior to the experiment, the cell is filled vertically before sealing with a semi-permeable mesh. Then, the cell is rotated vertically so that the grains free fall to the other end of the cell without any external effect. This enables that the solid ratio is very close to the random loose packing with a solid fraction of ϕ = 0.44±0.04 [*Eriksen et al.*, 2017b]. Finally, the cell is carefully placed horizontally without changing this loose state. This simple preparation procedure ensures that the experiments are reproducible. An empty space is provided between the air inlet and the solid-air interface to provide a homogenous pressure over the width of the cell. The air overpressure at the inlet is then raised and maintained at a constant level (1 bar in the example on Figure 1).

During this experiment, acoustic signals are recorded using 4 accelerometers attached to the bottom plate (see Figure 1(b)). The sensors are placed towards the outlet (where most of the stick-slip events are happening) to have a better signal resolution. The sensors are Miniature piezoelectric charge accelerometer 4374 - Brüel & Kjaer associated

to a NEXUS Charge Amplifier - Type 2692-A conditioner, and the signal is digitized using a National Instruments NI-DAQ mx acquisition card PCI-6133 8 Channels acquisition card. The accelerometers have 1 Hz to 26 kHz flat response. Using the function given by the manufacturer the response is flattened up to 200 kHz. These accelerometers can record only normal direction to the glass plate. Depending on the sign of the cumulative displacement (positive or negative) recorded at the sensor we mark the corresponding signals with the polarisation up or down respectively. The acoustic events are located using ESEH for a certain window of the signal which starts at the arrival time and ends somewhere in the coda. We have presented a more detailed discussion linking the acoustic signal polarization to medium deformation in Supplementary Text S1. More information about time windowing can be obtained from Supplementary Figure S1 and associated caption. Furthermore, the procedure of detecting the acoustic events from raw recordings is described in the Supplementary Text S2.

3 Estimation of Source Energy Homogeneity (ESEH)

Estimation of Source Energy Homogeneity considers that the source energy calculated from different recordings should be the same after the correction of energy loss due to the travel-path attenuation (based on material and distance). If we express the source energy with E_s and consider that the energy spread cylindrically on the plates the recorded energy E_n at receiver n at a distant R can be expressed with $E_n = \frac{E_s}{2\pi R h}$ where h is the plate thickness. E_s can be estimated following *Hibert et al.* [2011]; *Farin et al.* [2016]; *Turkaya et al.* [2016] by:

$$E_s(\mathbf{r_s}, \mathbf{r_n}) = \int_0^{\omega_{Nyq}} 2\pi R(n)\rho hc(\omega)\frac{|a(\omega)|^2}{\omega^2}d\omega, \tag{1}$$

where $E_s(\mathbf{r_s}, \mathbf{r_n})$ is the computed energy coming from a source at $\mathbf{r_s}$ recorded by a sensor at $\mathbf{r_n}$. ρ is the mass density of the plate, $c(\omega)$ is the group velocity of the waves over different angular frequencies ω up to Nyquist frequency ω_{Nyq}, $a(\omega)$ is the Fourier transform of the accelerometric recordings. $R(n) = ||\mathbf{r_n} - \mathbf{r_s}||$ is the distance between the source and the receiver and h is the plate thickness. Depending on the plate material there could be a viscous attenuation factor $e^{(2\gamma(\omega)R(n))}$ added to the right side of the Eq. (1) to account for viscous energy losses where $\gamma(\omega)$ is the viscous attenuation inverse distance. However, for glass plates and the distances that are used in this experiment viscous attenuation can be neglected (i.e. $\gamma \approx 0$ [*Farin et al.*, 2015]). In the experimental setup, 4 sensors are placed on the bottom glass plate on different locations (see Figure 1b and c) to have a good spa-

tial coverage. Standard deviation $\sigma(\mathbf{r_s})$ for source energy E_s at different test positions $\mathbf{r_s}$ on a regular grid for 4 different sensors are calculated. The minimum of this standard deviation indicates over all tested positions $\mathbf{r_s}$ the source location [*Turkaya et al.*, 2016]. We used 5 mm grid spacing for the trial positions $\mathbf{r_s}$ on the 45 cm × 30 cm area covered by the porous medium inside the Hele-Shaw cell.

4 Image processing for deformation localization

The optical images were captured via a high-speed camera (FastCam SA5 - Photron, recorded with 125 or 1000 fps with a resolution 1024 × 1024 pixels) during the experiments. These images are investigated to localize the deformation corresponding to the time interval when the acoustic signal is emitted. The deformation of the medium during the acoustic emission is analyzed based on the image analysis techniques eventually producing frame-to-frame displacement fields of the porous medium [*Eriksen et al.*, 2015, 2017b,a; *Niebling et al.*, 2010; *Travelletti et al.*, 2012; *Chevalier et al.*, 2009].

First, two successive images corresponding to the start and the end of the acoustic event is taken. Following this pre-treatment, a Digital Image Correlation (DIC) procedure, called Ncorr (an open source 2D digital image correlation MATLAB software) is applied to obtain frame-to-frame displacement fields. Ncorr cross-correlates subwindows between two images to find displacement fields in between. A detailed description of Ncorr is given in *Blaber et al.* [2015].

In Figure 2(a), an example of the displacement magnitude field obtained is given in the background. This map shows the magnitude of the absolute displacement of the medium (without any defined direction in the format of $||\bar{u}|| = \sqrt{u_x^2 + u_y^2}$ where $u_{x,y}$ are the displacements in directions x and y) occurring between two images taken at 8 ms from each other. The colormap shows the norm of the displacement field over the Hele-Shaw cell. As it can be seen for this snapshot, the displacements are focused on the fingertips. However, it is still possible to see nonzero displacements (of lower amplitudes) farther from the fingertips into the porous medium.

5 Results and Discussion

In Figure 2 the localization for an acoustic event is given. Displacement maps (in grey) are overlaid by acoustic localization results. Markers with different colors are calcu-

lated for different time window lengths to define the primary signal (see Supplementary Figure S1 for window lengths). The size of the time window is set to extend stepwise to give multiple estimations for a single event for a better comparison with DIC results. DIC gives us an idea about the evolution of the signal location by indicating the location of the displacement occurred during this time interval. In Figure 2 we see that the event source starts inside the porous medium and progresses towards the channel tips. Moreover, by increasing the size of the time window of the signal, we increase the sensitivity of the sensors for the waves coming from a larger area. The waves propagating on thin plates - similar to the glass plates which are used in this experimental study - may propagate at different velocities as a function of their frequency, which is the definition of dispersive waves. In this work, the "dispersivity" of the Lamb Waves are taken into account in wave velocity calculations using experimental and theoretical computations [*Royer and Dieulesaint*, 2000].

We increase the temporal resolution of the high-speed camera to record these events in more details. In Figure 3, compared to the displacement magnitude given in Figure 2(a) we increased the temporal resolution to 1000 frames per second (initially 125 fps). Moreover, to increase the spatial resolution of the images (and the resulting displacement maps) we are focusing on sub-parts of the Hele-Shaw cell where most of the grain displacement takes place. These settings allow us to follow the stick-slip events using the optical equipment with higher spatial and temporal resolution. In Figure 3(b) we see the location of the analyzed area in the cell (the channels are white, the granular porous medium is black, the analyzed part of the medium is grey).

Figure 3(b) also shows us how this stick-slip event starts inside the zone being compacted around 20 cm away from the tip of the channels with a decompacting zone behind, and the pulse, pair of compacting zone and decompacting zone behind, travels backward towards the fingertip (in a direction opposite to the grains direction) propagates towards the tip of the channels. This is very similar to the phenomenon that we observed in Figure 2(a) where the source of the microseismic emission starts inside the porous medium and progresses towards the channel tips (see the encircled zone). The first part of the signal is more sensitive to the start of the event than the whole slip event. Hence, they locate the equivalent of the epicenter, which is typically ahead of the fingers, as illustrated in Figure 3. Later on, the displacement gets distributed around most of the fingertips, and ends up with the slip of the grains around the tips. The ESEH method is more sensitive

to observe this evolution than the conventional arrival-time-based seismic location methods since the arrival time of the event does not vary with time but the energy emitted per second does. As the time window gets enlarged, the sensors are more and more sensitive to signals coming from a larger and larger area, and the resulting location, which considers that the source is point-like in the methods, seems to come approximately from points belonging to the mobile region, closer to the fingertips.

6 Conclusion

In this article, we show that the digital images and acoustic signals are very good (and coherent) monitoring tools to detect and localize fracturing and channeling in a porous medium. Different acoustic events having different natures (and locations) are investigated optically and acoustically (see Supplementary Figures S5-27 for more events and corresponding event recordings). The deformation magnitude maps obtained from digital image correlation method are compared with the acoustic signal based source localization results. The size of the time windows was set to extend freely so that the method would give multiple results for a single event for a better comparison. Depending on the polarization found on different sensors, it is possible to define the type of the source leading acoustic emissions. Localization results seem to fit well with displacement map obtained from the optical analysis techniques.

Acknowledgments

We would like to thank Alain Steyer and Miloud Talib for the technical support. This project has received funding from the European Union's Seventh Framework Programme for research under grant agreement no 316889 - FLOWTRANS, INSU ALEAS TelluS program, the International Associate Laboratory France-Norway on Deformation Flow and fracture of disordered Materials LIA D-FFRACT, from the Universities of Oslo and Strasbourg via a gjesteforsker program and an IDEX Espoirs award. Furthermore, this work was partly supported by the Research Council of Norway through its Centres of Excellence funding scheme, project number 262644 and grant 213462/F20. The experimental dataset and the Matlab routines used in this study can be found on www.doi.org/10.5281/zenodo.1316548

References

Accutech (1994), *Accutech Pneumatic Fracturing Extraction and Hot Gas Injection, Phase One: Applications Analysis Report*, DIANE Publishing Company.

Aki, K., and P. G. Richards (2002), *Quantitative Seismology, 2nd Ed.*, University Science Books.

Allen, R. V. (1978), Automatic earthquake recognition and timing from single traces, *Bulletin of the Seismological Society of America*, *68*(5), 1521–1532.

Aochi, H., B. Poisson, R. Toussaint, and J. Schmittbuhl (2011), Induced seismicity along a fault due to fluid circulation: conception and application, in *Japan Geoscience Union Meeting 2011, May 2011, Makuhari, Chiba, Japan*.

Baer, M., and U. Kradolfer (1987), An automatic phase picker for local and teleseismic events, *Bulletin of the Seismological Society of America*, *77*(4), 1437–1445.

Blaber, J., B. Adair, and A. Antoniou (2015), Ncorr: open-source 2d digital image correlation matlab software, *Experimental Mechanics*, *55*(6), 1105–1122.

Brandstein, M., J. Adcock, and H. Silverman (1997), A closed-form location estimator for use with room environment microphone arrays, *Speech and Audio Processing, IEEE*, *5*(1), 45–50, doi:10.1109/89.554268.

Butterworth, S. (1930), On the theory of filter amplifiers, *Wireless Engineer*, *7*(6), 536–541.

Candela, T., B. Wassing, J. Ter Heege, and L. Buijze (2018), How earthquakes are induced, *Science*, *360*(6389), 598–600.

Charléty, J., N. Cuenot, L. Dorbath, C. Dorbath, H. Haessler, and F. M. (2007), Large earthquakes during hydraulic stimulations at the geothermal site of soultz-sous-forets, *International Journal of Rock Mechanics and Mining Sciences*, *44*(8), 1091 – 1105, doi: http://dx.doi.org/10.1016/j.ijrmms.2007.06.003.

Chevalier, C., A. Lindner, M. Leroux, and E. Clément (2009), Morphodynamics during air injection into a confined granular suspension, *Journal of Non-Newtonian Fluid Mechanics*, *158*(1), 63–72.

Christenson, B., A. Reyes, R. Young, A. Moebis, S. Sherburn, J. Cole-Baker, and K. Britten (2010), Cyclic processes and factors leading to phreatic eruption events: Insights from the 25 september 2007 eruption through ruapehu crater lake, new zealand, *Journal of Volcanology and Geothermal Research*, *191*(1-2), 15–32.

278 Cornet, F. (2015), *Elements of Crustal Geomechanics*, Cambridge University Press.

279 Cornet, F., J. Helm, H. Poitrenaud, and A. Etchecopar (1998), Seismic and aseismic slips
280 induced by large-scale fluid injections, in *Seismicity Associated with Mines, Reservoirs*
281 *and Fluid Injections*, pp. 563–583, Springer.

282 Cuenot, N., C. Dorbath, and L. Dorbath (2008), Analysis of the microseismicity induced
283 by fluid injections at the egs site of soultz-sous-forets (alsace, france): Implications
284 for the characterization of the geothermal reservoir properties, *Pure and Applied Geo-*
285 *physics*, *165*(5), 797–828, doi:10.1007/s00024-008-0335-7.

286 Dorbath, L., N. Cuenot, A. Genter, and M. Frogneux (2009), Seismic response of the
287 fractured and faulted granite of soultz-sous-forets (france) to 5 km deep massive wa-
288 ter injections, *Geophysical Journal International*, *177*(2), 653–675, doi:10.1111/j.1365-
289 246X.2009.04030.x.

290 Earle, P. S., and P. M. Shearer (1994), Characterization of global seismograms using an
291 automatic-picking algorithm, *Bulletin of the Seismological Society of America*, *84*(2),
292 366–376.

293 Elnahrawy, E., X. Li, and R. Martin (2004), The limits of localization using signal
294 strength: a comparative study, in *Sensor and Ad Hoc Communications and Networks,*
295 *IEEE*, pp. 406–414, doi:10.1109/SAHCN.2004.1381942.

296 Eriksen, F. K., R. Toussaint, K. J. Måløy, and E. G. Flekkøy (2015), Invasion patterns
297 during two-phase flow in deformable porous media, *Frontiers in Physics*, *3*, 81.

298 Eriksen, F. K., R. Toussaint, A. L. Turquet, K. J. Måløy, and E. G. Flekkøy (2017a), Pres-
299 sure evolution and deformation of confined granular media during pneumatic fracturing
300 (in review), *Phys. Rev. E*.

301 Eriksen, F. K., R. Toussaint, A. L. Turquet, K. J. Måløy, and E. G. Flekkøy (2017b),
302 Pneumatic fractures in confined granular media, *Phys. Rev. E*, *95*, 062,901, doi:
303 10.1103/PhysRevE.95.062901.

304 Eriksen, F. K., R. Toussaint, A. L. Turquet, K. J. Måløy, and E. G. Flekkøy (2018), Pres-
305 sure evolution and deformation of confined granular media during pneumatic fracturing,
306 *Phys. Rev. E*, *97*, 012,908, doi:10.1103/PhysRevE.97.012908.

307 Farin, M., A. Mangeney, R. Toussaint, J. de Rosny, N. Shapiro, T. Dewez, C. Hibert,
308 C. Mathon, O. Sedan, and F. Berger (2015), Characterization of rockfalls from seismic
309 signal: insights from laboratory experiments, *JGR: Solid Earth*, *120*(10), 7102–7137.

Farin, M., A. Mangeney, J. De Rosny, R. Toussaint, J. Sainte-Marie, and N. Shapiro (2016), Experimental validation of theoretical methods to estimate the energy radiated by elastic waves during an impact, *Journal of Sound and Vibration*, *362*, 176–202.

Fehler, M., L. House, and H. Kaieda (), Determining planes along which earthquakes occur: Method and application to earthquakes accompanying hydraulic fracturing, *Journal of Geophysical Research: Solid Earth*, *92*(B9), 9407–9414, doi:10.1029/JB092iB09p09407.

Fink, M. (2015), Acoustic imaging with time reversal methods: From medicine to ndt, *AIP Conference Proceedings*, *1650*(1), 13–23, doi:http://dx.doi.org/10.1063/1.4914591.

Gao, F., H. Xie, F. Zhou, Y. Ju, L. Xie, Y. Liu, Y. Gao, J. Liu, and R. Zhang (2014), Pneumatic fracturing method and system for exploiting shale gas, uS Patent App. 14/335,935.

Garnier, J., and M. Fink (2015), Super-resolution in time-reversal focusing on a moving source, *Wave Motion*, *53*, 80 – 93, doi:http://dx.doi.org/10.1016/j.wavemoti.2014.11.005.

Gershman, A., V. Turchin, and V. Zverev (1995), Experimental results of localization of moving underwater signal by adaptive beamforming, *Signal Processing, IEEE*, *43*(10), 2249–2257, doi:10.1109/78.469863.

Häring, M. O., U. Schanz, F. Ladner, and B. C. Dyer (2008), Characterisation of the basel 1 enhanced geothermal system, *Geothermics*, *37*(5), 469–495.

Hibert, C., A. Mangeney, G. Grandjean, and S. Nikolai (2011), Slope instabilities in Dolomieu crater, Réunion Island: From seismic signals to rockfall characteristics, *Journal of Geophysical Research - earth surface*, *116*, F04,032, doi:10.1029/2011JF002038.

Holland, A. A. (2013), Earthquakes triggered by hydraulic fracturing in south?central oklahomaearthquakes triggered by hydraulic fracturing in south?central oklahoma, *Bulletin of the Seismological Society of America*, *103*(3), 1784, doi:10.1785/0120120109.

Jamtveit, B., Y. Ben-Zion, F. Renard, and H. Austrheim (2018), Earthquake-induced transformation of the lower crust, *Nature*, *556*(7702), 487–491, doi:10.1038/s41586-018-0045-y.

Jolly, A., P. Jousset, J. Lyons, R. Carniel, N. Fournier, B. Fry, and C. Miller (2014), Seismo-acoustic evidence for an avalanche driven phreatic eruption through a beheaded hydrothermal system: An example from the 2012 tongariro eruption, *Journal of Volcanology and Geothermal Research*, *286*, 331 – 347, doi:https://doi.org/10.1016/j.jvolgeores.2014.04.007.

Kobchenko, M., A. Hafver, E. Jettestuen, O. Galland, F. Renard, P. Meakin, B. Jamtveit, and D. K. Dysthe (2013), Drainage fracture networks in elastic solids with internal fluid generation, *EPL (Europhysics Letters)*, *102*(6), 66,002.

Malioutov, D., M. Cetin, and A. Willsky (2005), A sparse signal reconstruction perspective for source localization with sensor arrays, *Signal Processing, IEEE*, *53*(8), 3010–3022, doi:10.1109/TSP.2005.850882.

Manga, M., and E. Brodsky (2006), Seismic triggering of eruptions in the far field: Volcanoes and geysers, *Annu. Rev. Earth Planet. Sci*, *34*, 263–291.

Niebling, M. J., E. G. Flekkøy, K. J. Måløy, and R. Toussaint (2010), Mixing of a granular layer falling through a fluid, *Physical Review E - Statistical, Nonlinear, and Soft Matter Physics*, *82*(1).

Oppenheimer, D. H. (1986), Extensional tectonics at the geysers geothermal area, california, *Journal of Geophysical Research: Solid Earth*, *91*(B11), 11,463–11,476.

Peacock, M. (1996), Acoustic emission for detection of process-related damage in pressure vessels and piping, pp. 2947 – 2947 – 9, doi:10.1117/12.259158.

Poland, M. P., A. Miklius, A. J. Sutton, and C. R. Thornber (2012), A mantle-driven surge in magma supply to kīlauea volcano during 2003–2007, *Nature Geoscience*, *5*(4), 295.

Rivalta, E., and P. Segall (2007), Magma compressibility and the missing source for some dike intrusions, *Geophysical Research Letters*, *35*(4), doi:10.1029/2007GL032521.

Royer, D., and E. Dieulesaint (2000), *Elastic Waves in Solids I: Free and Guided Propagation*, Advanced Texts in Physics, Springer.

Schuring, J., D. Kosson, C. Fitzgerald, and S. Venkatraman (1996), Pneumatic fracturing and multicomponent injection enhancement of in situ bioremediation, uS Patent 5,560,737.

Stanchits, S., S. Mayr, S. Shapiro, and G. Dresen (2011), Fracturing of porous rock induced by fluid injection, *Tectonophysics*, *503*(1), 129 – 145, doi: https://doi.org/10.1016/j.tecto.2010.09.022, thermo-Hydro-Chemo-Mechanical Couplings in Rock Physics and Rock Mechanics.

Sudo, Y., H. Ono, A. W. Hurst, T. Tsutsui, T. Mori, M. Nakaboh, Y. Matsumoto, M. Sako, S. Yoshikawa, M. Tanaka, Y. Kobayashi, T. Hashimoto, T. Hoka, T. Yamada, H. Masuda, and S. Kikuchi (1998), Seismic activity and ground deformation associated with 1995 phreatic eruption of kuju volcano, kyushu, japan, *Journal of Volcanology and Geothermal Research*, *81*(3), 245 – 267, doi:https://doi.org/10.1016/S0377-

0273(98)00011-0.

Tazieff, H. (1989), Mechanisms of the nyos carbon dioxide disaster and of so-called phreatic steam eruptions, *Journal of volcanology and geothermal research*, *39*(2-3), 109–116.

Terlizzi, J., and J. Minoo (2009), Multi-touch display screen with localized tactile feedback, uS Patent App. 12/069,352.

Travelletti, J., C. Delacourt, P. Allemand, J.-P. Malet, J. Schmittbuhl, R. Toussaint, and M. Bastard (2012), Correlation of multi-temporal ground-based optical images for landslide monitoring: Application, potential and limitations, *{ISPRS} Journal of Photogrammetry and Remote Sensing*, *70*(0), 39 – 55, doi: http://dx.doi.org/10.1016/j.isprsjprs.2012.03.007.

Trnkoczy, A. (1998), Understanding & setting sta/lta trigger algorithm parameters for the k2, *Application Note*, *41*, 16–20.

Turkaya, S., R. Toussaint, F. K. Eriksen, M. Zecevic, G. Daniel, E. G. Flekkøy, and K. J. Måløy (2015), Bridging aero-fracture evolution with the characteristics of the acoustic emissions in a porous medium, *Frontiers in Physics*, *3*, 70.

Turkaya, S., R. Toussaint, F. K. Eriksen, O. Lengliné, G. Daniel, E. G. Flekkøy, and K. J. Måløy (2016), Note: Localization based on estimated source energy homogeneity, *Review of Scientific Instruments*, *87*(9), 096,101.

Turquet, A., T. Bodin, P. Arroucau, M. Sylvander, and K. Manchuel (2018a), Quantifying the seismic location uncertainties in french seismicity catalogues: Application to the pyrenees (in prep), *Seismological Research Letters*.

Turquet, A. L., R. Toussaint, F. K. Eriksen, G. Daniel, D. Koehn, and E. G. Flekkøy (2018b), Microseismic emissions during pneumatic fracturing: A numerical model to explain the experiments, *Journal of Geophysical Research: Solid Earth*, *123*(8), 6922–6939, doi:10.1029/2017JB014613.

Valin, J., F. Michaud, J. Rouat, and D. Letourneau (2003), Robust sound source localization using a microphone array on a mobile robot, in *IROS 2003. Proceedings. IEEE/RSJ*, vol. 2, pp. 1228–1233 vol.2, doi:10.1109/IROS.2003.1248813.

Valkó, P., and M. Economides (1995), *Hydraulic fracture mechanics*, Wiley.

Wong, J., L. Han, J. Bancroft, and R. Stewart (2009), Automatic time-picking of first arrivals on noisy microseismic data, *CSEG. 0 0.2 0.4 0.6 0.8*, *1*(1.2), 1–4.

408 Zhu, Q., S. Tannenbaum, and S. H. Kurtzman (2007), Optical tomography
409 with ultrasound localization for breast cancer diagnosis and treatment mon-
410 itoring, *Surgical Oncology Clinics of North America*, *16*(2), 307 – 321, doi:
411 http://dx.doi.org/10.1016/j.soc.2007.03.008, pre and Postoperative Cancer Imag-
412 ing:Practical and Innovative Approaches.

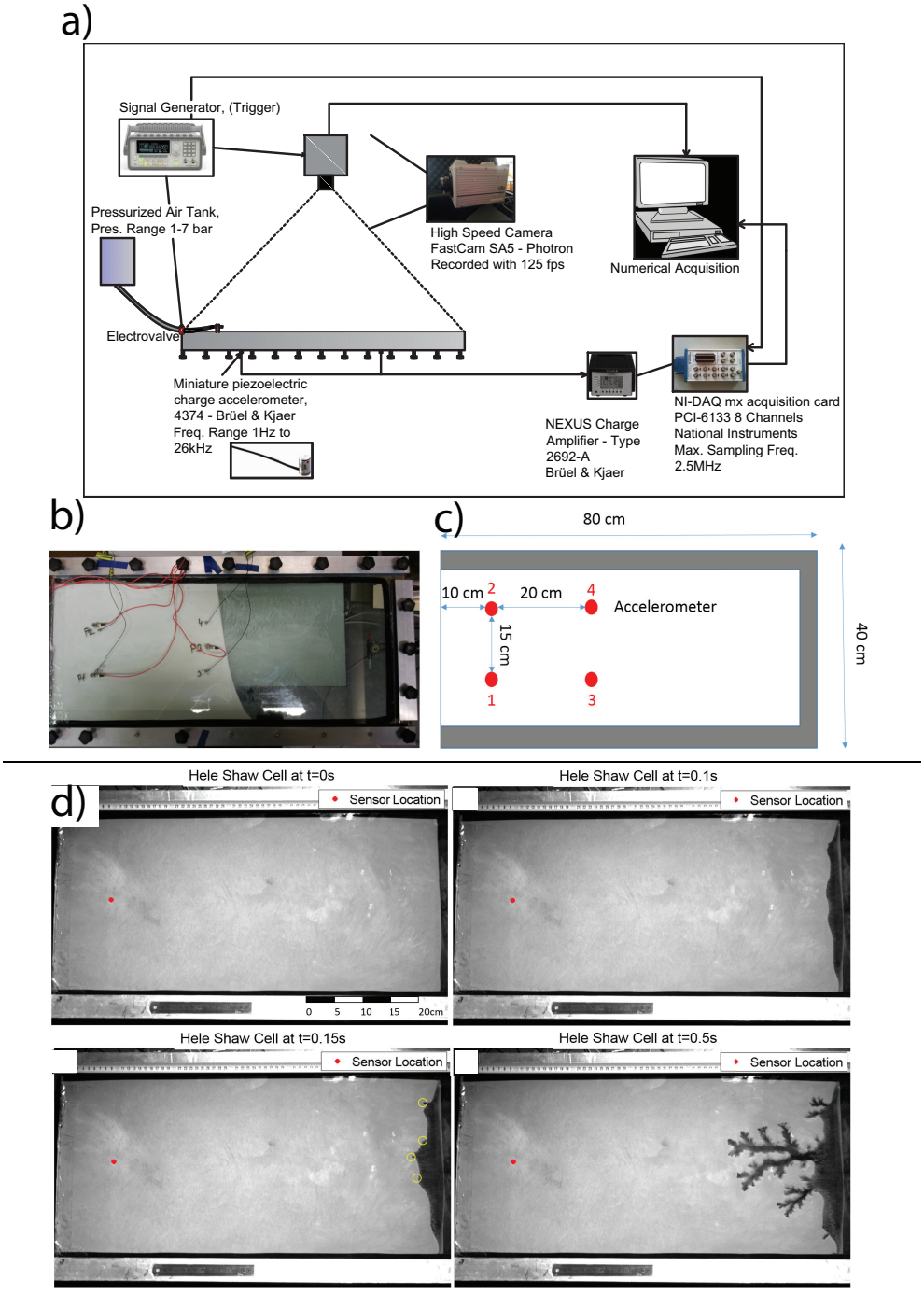

Figure 1. (a) The acquisition chain of the aero-fracturing experiments with a Hele-Shaw cell. The signal acquisition card, camera and the electrovalve connected to the air pump are triggered at the same time via a TTL signal sent from the signal generator to have synchronized optical and acoustic data. The sensors are placed on the bottom glass plate of the Hele-Shaw cell using a solid crystallized phenyl salicylate. (b) The image showing the accelerometers stick under the Hele-Shaw cell is given. In (c), accelerometers are sketched and numbered. Red dots show the positions of the accelerometers. (d) We present several snapshots of the cell during injection.

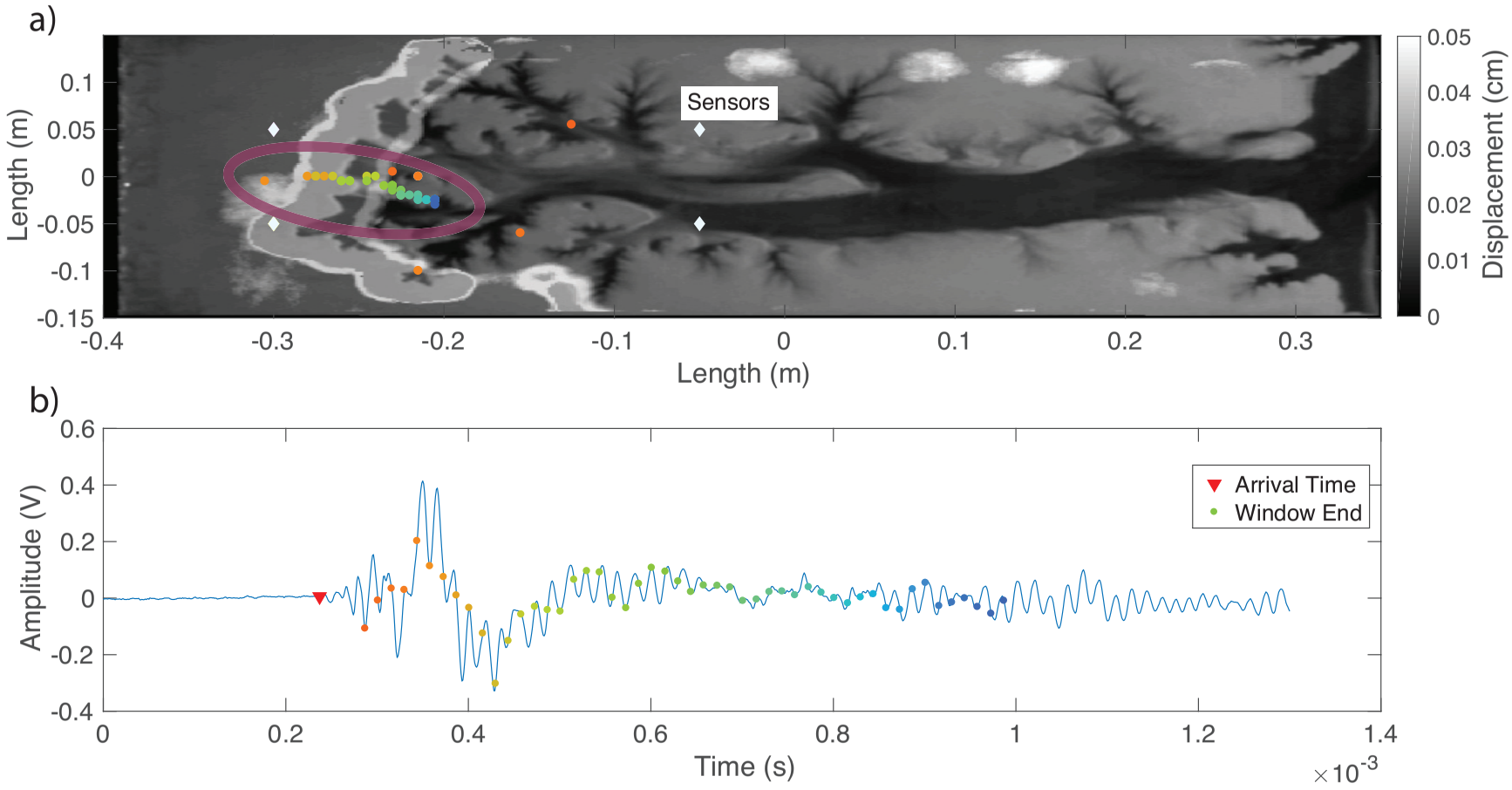

Figure 2. Localization of an acoustic event. (a): The localized source and receiver positions are indicated. Diamond markers show the accelerometer locations. The circle markers with different colors show the ESEH results with different input signal lengths starting from the red triangle at (b) and ending at the associated colored dot. The grayscale bar indicates the optically computed displacement magnitude in cm. (b): The acoustic event with different window sizes are presented. The red triangle shows the picked arrival time, which is the start of the signal for all time windows. The colored dots are the different ends of all windows used, resulting in different locations shown in (a).

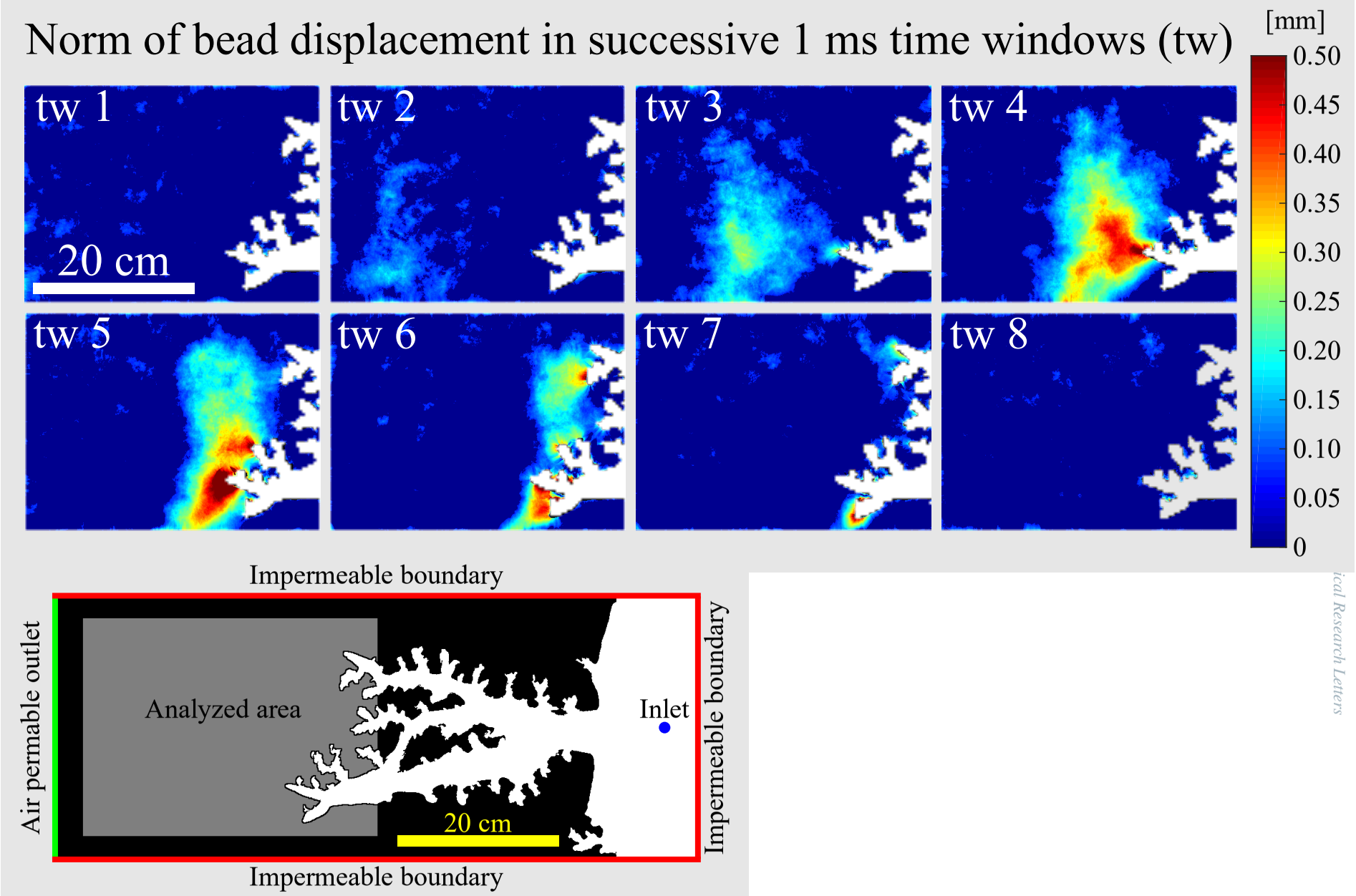

Figure 3. a) Displacement magnitude (mm) in successive time windows (tw). The image set covers 8 ms. b) Sketch of the Hele-Shaw cell and the location of the analyzed area.